

Simulation of the Heston stochastic local volatility model: implicit and explicit approaches*

Meng Cai ^a and Tianze Li ^{b †}

^a School of Statistics and Mathematics, Central University of Finance and Economics, Beijing, China

^b School of Economics, Central University of Finance and Economics, Beijing, China

September 30, 2025

Abstract

The Heston stochastic-local volatility (HSLV) model is widely used to capture both market calibration and realistic volatility dynamics, but simulating its CIR-type variance process is numerically challenging. This paper compares two alternative schemes for HSLV simulation: the truncated Euler method and the backward Euler method with the conventional Euler and almost exact simulation methods in [22] by using a Monte Carlo method. Numerical results show that the truncated method achieves strong convergence and remains robust under high volatility, while the backward method provides the smallest errors and most stable performance in stress scenarios, though at higher computational cost.

Key Words: Heston stochastic-local volatility model, truncated Euler method, backward Euler method

1 Introduction

The evolution of financial models is essentially aimed at resolving the core contradictions in pricing and risk management. The birth of the SLV model is to address a fundamental problem in financial engineering, namely the trade-off between perfect calibration and correct dynamics. The Local Volatility (LV) model proposed by Dupire [9] and Derman & Kani [8] was widely used for a long time. This model can be designed to fully fit the implied volatility surface of all European options in the current market. This is a very powerful feature, ensuring the model's no-arbitrage consistency with the market prices observed "today". However, its drawback is that there are problems with the future volatility behavior predicted by the LV model. It usually generates a flattened forward volatility smile [17]. This means that if the underlying asset price changes

*This work was supported by the National Natural Science Foundation of China (No. 12501581) and the Disciplinary Funding of Central University of Finance and Economics.

†Corresponding author: litianze6@126.com

significantly in the future, the model assumes that the future implied volatility will tend to be flat, which seriously contradicts the actual market observations (such as the continuous pricing of tail risks in the options market). This can lead to mispricing and incorrect hedging of path-dependent products (such as forward-starting options, step options, and snowball options). The advantage of the Stochastic Volatility (SV) model proposed in [13] and [20], represented by the Heston model, is that its volatility is stochastic and has its own movement rules. It can naturally generate and maintain the shape of the volatility smile/skew extending into the future, and the forward volatility dynamics it predicts are more in line with market common sense. Therefore, in theory, it can price the above-mentioned complex derivatives more accurately. Nevertheless, the standard Heston model has limited parameters, making it difficult to perfectly fit the implied volatility for all tenors and strike prices simultaneously. In particular, it usually has insufficient ability to fit the smile of short-term options [11]. An “imperfect” calibration means that the model cannot even accurately reproduce today’s market prices, which undermines the foundation of its pricing. Then the SLV model emerged [15]. It allows the stochastic volatility (SV) component to drive the correct dynamics of volatility and the local volatility (LV) component to act as a compensator, responsible for correcting the fitting errors of the SV model to the current market prices. This combination enables the model to leverage the advantages of both approaches, making it a powerful pricing tool in the finance industry. Indeed, an SLV model outperforms a pure LV or SV model in calibrating European options, pricing, and risk management (see, e.g., [12, 16, 18, 21, 22]).

In the SLV simulation process, the simulation of the volatility process serves as the foundation for all predictions. However, simulating the CIR process is extremely tricky. Although there has been a few works [5, 6, 7, 14], it is still far from being well-understood. The core challenge lies in its diffusivity. Even when the Feller condition is met, $V(t)$ in numerical simulations can easily reach negative values due to Brownian motion. A negative variance is meaningless both mathematically and financially, which can cause the entire simulation to collapse. Previous studies in numerical simulations either take the maximum of V and 0 at each step to ensure non-negativity, or use the non-central chi-square distribution and only achieve convergence in the sense of distribution. We explore new simulation methods by borrowing new mathematical research, and then observe the improvement in the overall option pricing to meet the requirements of different option applications.

The article is organized as follows. In the next section, we present the background and give a brief introduction to the underlying model. We then introduce and analyse the numerical schemes in Section 3. The corresponding proofs are given in the Appendix. Section 4 provides numerical experiment to confirm the theoretical findings.

2 The considered model

For a given time horizon $[0, T]$, we consider a complete filtered probability space $(\Omega, \mathcal{F}, \mathbb{P})$ with natural filtration $(\mathcal{F}_t)_{t \in [0, T]}$, which supports an \mathcal{F}_t -adapted two-dimensional standard Brownian motion (W_t, \widetilde{W}_t) . In this article, we consider the HSLV model

$$\begin{cases} dS_t = rS_t dt + \sqrt{V_t} S_t \sigma(t, S_t) \left(\rho dW_t + \sqrt{1 - \rho^2} d\widetilde{W}_t \right), & S_0 > 0, \\ dV_t = \underbrace{\kappa}_{\gamma} (\theta - V_t) dt + \gamma \sqrt{V_t} dW_t, & V_0 > 0, \\ dW_t d\widetilde{W}_t = \rho dt, & \rho \in (0, 1), \end{cases} \quad (2.1)$$

where S_t is the value at time t of the one-dimensional process $S = (S_t)_{t \in [0, T]}$ describing the spot price of the underlying asset, and V_t is the value at time t of the squared volatility process $V = (V_t)_{t \in [0, T]}$.

In order to calibrate this model to market prices, it is common to follow two steps. First, we use a set of observed call option prices from the market to calibrate a pure Heston process. This helps us determine the parameters under which the model best aligns with the market prices. There is a semi-closed form solution for the price as a function of the parameters, and we can find the optimal parameters by numerically solving a low-dimensional constrained optimisation problem. Second, at each step (t) of time-discretization, we need to calibrate the so-called leverage function ($\sigma(t, \cdot)$). For the exact calibration of SV models, a consistency condition to market prices is formulated in [9]. For general SLV models in [15],

$$\sigma^2(t, s) = \frac{\sigma_{\text{Dup}}^2(t, s)}{\mathbb{E}[V_t | S_t = s]}, \quad (2.2)$$

where σ_{Dup} is expressed by the Dupire formula, for given call option market prices $C(T, S)$ with maturity time T and strike S :

$$\sigma_{\text{Dup}}^2(T, S) = \left(\frac{\partial C(T, S)}{\partial T} + rS \frac{\partial C(T, S)}{\partial S} \right) / \left(\frac{S^2}{2} \cdot \frac{\partial^2 C(T, S)}{\partial S^2} \right),$$

where, we assume zero interest and dividend rates.

The volatility process has Cox–Ingersoll–Ross (CIR) dynamics [4] is formulated as

$$dV_t = \kappa(\theta - V_t)dt + \gamma \sqrt{V_t} dW_t, \quad V_0 > 0 \quad (2.3)$$

has parameters $\kappa, \theta, \gamma > 0$ describing its mean-reversion rate, long-term mean, and volatility, respectively. Let $2\kappa\theta \geq \sigma^2, T > 0$, then (2.3) admits a unique solution $X(t)$ satisfying

$$\mathbb{P}\{V_t > 0, \forall t > 0\} = 1$$

and

$$\sup_{0 \leq t \leq T} \mathbb{E}[|V_t|^p] \leq \infty, \quad p > -\frac{2\kappa\theta}{\sigma^2}.$$

The model (2.1) is well-received in the industry. It benefits from the useful characteristics of the CIR process, including mean reversion and non-negativity [1]. Additionally, the Heston model is analytically solvable, which enables the rapid calibration of its parameters.

3 The proposed numerical simulation

Fixed $T > 0, N \in \mathbb{N}_+$, step-size $\tau = \frac{T}{N}, t_n = n\tau, n = 0, 1, \dots, N$. For $m = 0, 1, 2, \dots, N - 1$, we denote $\Delta W_m = W_{t_{m+1}} - W_{t_m}$ for simplicity.

3.1 Simulation of volatility V_t

When applying the Euler–Maruyama method to CIR-type process, the variance process can become negative with a positive probability. To address this issue, we first apply Lamperti transformation $L_t = \sqrt{V_t}$ to (2.3) and give

$$dL_t = \frac{1}{2}\kappa \left(\frac{\theta}{L_t} - L_t \right) dt + \frac{1}{2}\sigma dW_t, \quad t \in (0, T], \quad L_0 = \sqrt{V_0}. \quad (3.1)$$

Next, we introduce two kinds of positivity-preserving numerical method.

3.1.1 Backward Euler method

The backward Euler method applied to (3.1) gives

$$L_{t_{n+1}}^N = L_{t_n}^N + \frac{\kappa}{2}\tau \left(\frac{\theta}{L_{t_{n+1}}^N} - L_{t_{n+1}}^N \right) + \frac{1}{2}\sigma\Delta W_n, \quad (3.2)$$

which has a unique positive solution

$$L_{t_{n+1}}^N = \frac{L_{t_n}^N + \frac{1}{2}\sigma\Delta W_n + \sqrt{(L_{t_n}^N + \frac{1}{2}\sigma\Delta W_n)^2 + \kappa\tau\theta(2 + \kappa\tau)}}{2 + \kappa\tau}. \quad (3.3)$$

This scheme is implicit and stable, but a nonlinear system is needed to solve at each step. In the following, we use truncating skill to get an explicit scheme [10].

3.1.2 Truncated Euler method

For any given $\tau \in (0, 1]$, the truncated mapping $\pi_\tau : \mathbb{R} \rightarrow \mathbb{R}$ is defined by

$$\pi_\tau(x) = (b\tau^{\frac{1}{4}}) \vee x, \quad \forall x \in \mathbb{R},$$

where $b \leq Y_0$ and is independent with the step-size τ . The so-called truncated Euler method is given as follows,

$$L_{t_{n+1}}^N = L_{t_n}^N + \frac{\kappa}{2}\tau \left(\frac{\theta}{\pi_\tau(L_{t_n}^N)} - \pi_\tau(L_{t_n}^N) \right) + \frac{1}{2}\sigma\Delta W_n. \quad (3.4)$$

By taking $\bar{L}_{t_n}^N = \pi_\tau(L_{t_n}^N)$, we derive a positive numerical solution for (3.1). We highlight that the truncated scheme with explicit time-stepping is more computationally efficient than the nonlinearity-implicit time-stepping, namely, backward Euler method.

Proposition 3.1. *Suppose $2\kappa\theta \geq \sigma^2, T > 0$. Then the numerical solution generated by the truncated Euler method strongly converges to the exact solution of (3.1).*

$$\sup_{1 \leq n \leq N} \left\| L_{t_n} - \bar{L}_{t_n}^N \right\|_{L^2(\Omega; \mathbb{R})} \leq C \tau^{\frac{1}{2}}. \quad (3.5)$$

Next, by inverse Lamperti transformation, we arrive at the following result.

Theorem 3.2. Under the assumption of Proposition 3.1, let $\bar{V}_t^N = \left(\sum_{k=1}^{\infty} \bar{L}_{t_k}^N \chi_{[t_{k-1}, t_k)}(t) \right)^2$, then for any $\tau \in (0, 1]$,

$$\sup_{1 \leq n \leq N} \mathbb{E} \left| V_{t_n}^N - \bar{V}_{t_n}^N \right| \leq C \tau^{\frac{1}{2}}. \quad (3.6)$$

3.2 Simulation of asset price S_t

For the asset price process, we follow [3] and give the discretization of $R_t := \log(S_t)$ with $\hat{\sigma}(t, R_t) := \sigma(t, e^{R_t})$, which reads

$$\begin{aligned} R_{t_{i+1}} = R_{t_i} &+ \int_{t_i}^{t_{i+1}} \left(r - \frac{1}{2} \hat{\sigma}^2(s, R_s) V_s \right) ds + \rho \int_{t_i}^{t_{i+1}} \hat{\sigma}(s, R_s) \sqrt{V_s} dW_s \\ &+ \sqrt{1 - \rho^2} \int_{t_i}^{t_{i+1}} \hat{\sigma}(s, R_s) \sqrt{V_s} d\tilde{W}_s. \end{aligned} \quad (3.7)$$

It follows from the volatility process that

$$\int_{t_i}^{t_{i+1}} \sqrt{V_s} dW_s = \frac{1}{\gamma} \left(V_{t_{i+1}} - V_{t_i} - \kappa \theta \tau + \kappa \int_{t_i}^{t_{i+1}} V_s ds \right). \quad (3.8)$$

Then, the second integral in (3.7) can be approximated as follows,

$$\begin{aligned} \int_{t_i}^{t_{i+1}} \hat{\sigma}(s, R_s) \sqrt{V_s} dW_s &\approx \hat{\sigma}(t_i, R_{t_i}) \int_{t_i}^{t_{i+1}} \sqrt{V_s} dW_s \\ &= \frac{1}{\gamma} \hat{\sigma}(t_i, R_{t_i}) \left(V_{t_{i+1}} - V_{t_i} - \kappa \theta \tau + \kappa \int_{t_i}^{t_{i+1}} V_s ds \right). \end{aligned} \quad (3.9)$$

For the third integral in (3.7), using the Itô isometry gives

$$\int_{t_i}^{t_{i+1}} \hat{\sigma}(s, R_s) \sqrt{V_s} d\tilde{W}_s \sim \left(\int_{t_i}^{t_{i+1}} \hat{\sigma}^2(s, R_s) V_s ds \right)^{\frac{1}{2}} \mathcal{N}(0, 1), \quad (3.10)$$

where $\mathcal{N}(0, 1)$ obeys the standard normal distribution. Furthermore, by the Euler discretization of all integrals with respect to time, we have

$$\begin{aligned} R_{t_{i+1}} &\approx R_{t_i} + \int_{t_i}^{t_{i+1}} \left(r - \frac{1}{2} \hat{\sigma}^2(s, R_s) V_s \right) ds \\ &+ \frac{1}{\gamma} \rho \hat{\sigma}(t_i, R_{t_i}) \left(V_{t_{i+1}} - V_{t_i} - \kappa \theta \tau + \kappa \int_{t_i}^{t_{i+1}} V_s ds \right) \\ &+ \sqrt{1 - \rho^2} \left(\int_{t_i}^{t_{i+1}} \hat{\sigma}^2(s, R_s) V_s ds \right)^{\frac{1}{2}} \mathcal{N}(0, 1) \\ &\approx R_{t_i} + r\tau - \frac{1}{2} \tau \hat{\sigma}^2(t_i, R_{t_i}) V_{t_i} + \frac{1}{\gamma} \rho \hat{\sigma}(t_i, R_{t_i}) (V_{t_{i+1}} - V_{t_i} - \kappa \theta \tau + \kappa \tau V_{t_i}) \\ &+ \sqrt{(1 - \rho^2) \tau \hat{\sigma}^2(t_i, R_{t_i}) V_{t_i}} \mathcal{N}(0, 1). \end{aligned} \quad (3.11)$$

3.3 Simulation of $\sigma^2(t, S)$

The discrete scheme becomes

$$R_{i+1,j} = R_{i,j} + r\tau - \frac{1}{2}\tau\hat{\sigma}^2(t_i, R_{i,j})V_{i,j} + \sqrt{1 - \rho^2} \cdot \sqrt{\hat{\sigma}^2(t_i, R_{i,j})V_{i,j}\tau} \cdot \mathcal{N}(0, 1) + \frac{1}{\gamma}\rho\hat{\sigma}(t_i, R_{i,j})(V_{i+1,j} - V_{i,j} - \kappa\theta\tau + \kappa\tau V_{i,j}). \quad (3.12)$$

For the discretization of volatility, we employ the following approximation

$$\hat{\sigma}^2(t_i, R_{i,j}) := \sigma^2(t_i, e^{R_{i,j}}) = \frac{\sigma_{LV}^2(t_i, S_{i,j})}{\mathbb{E}[V_{t_i}|S_{t_i} = S_{i,j}]}, \quad (3.13)$$

where

$$\sigma_{LV}^2(t_i, S_{i,j}) = \left. \frac{\frac{\partial C(t,S)}{\partial t} + rS\frac{\partial C(t,S)}{\partial S}}{\frac{1}{2}S^2\frac{\partial^2 C(t,S)}{\partial S^2}} \right|_{S=S_{i,j}, t=t_i}. \quad (3.14)$$

When computing local volatility, the finite difference method is adopted. To mitigate deviations caused by excessively small second-order derivative results, a lower bound is implemented in the calculation process to enhance stability.

4 Numerical experiments

We perform some numerical experiments in this section to visually confirm our theoretical conclusion.

In our model setup, we primarily conduct numerical experiments on the HSLV model, using the standard Monte Carlo approach. The market environment is based on the classical Heston model, with the following parameters: $\gamma = 0.95$ (vol-of-vol), $\kappa = 1.05$ (mean reversion rate), $\rho = -0.315$ (correlation), $v\text{Bar} = 0.0855$ (long-run variance), $S_0 = 1.0$, $r = 0$, $v_0 = 0.0945$ (initial variance), and $T = 5$. For the HSLV model, which requires continuous adjustment, we introduce a modification parameter $p = 0.25$. The adjusted parameters are defined as follows: $\gamma\text{Model} = (1 - p) * \gamma$, $\kappa\text{Model} = (1 + p) * \kappa$, $\rho\text{Model} = (1 + p) * \rho$, $v\text{BarModel} = (1 - p) * v\text{Bar}$, $v\text{Model} = (1 + p) * v_0$, with $r = 0$, $S_0 = 1$, and $T = 5$.

Before starting the experiment, we first examined the ability of the Truncated and Backward methods to compute conditional expectations, ensuring that the binning approach could be reasonably applied to the calculation of volatility, consistent with the description in [2]. In testing conditional expectations, we used the 2D-COS method [19] as the benchmark. In the parameter settings, we chose 20 bins, 10,000 paths, and a step size of 0.001.

From Fig. 1, it can be observed that both the Truncated method and the Backward method effectively use the binning approach to estimate the conditional expectation, thereby ensuring the validity of our subsequent experiments. For the numerical experiments, in order to highlight the differences more clearly, we amplified the error by a factor of 100. The results are shown in the tables.

When the number of steps is small, the Truncated method typically exhibits the lowest error, which we attribute to its strong convergence properties. However, as the number of steps increases,

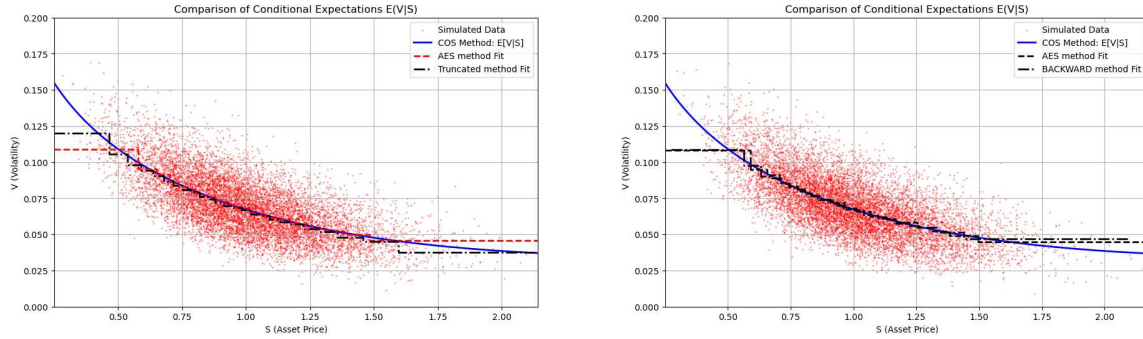


Figure 1: Comparison of expectations

Table 1: The error of four methods

N	$K = 70\%$			
	<i>Euler</i>	<i>AES</i>	<i>Truncated</i>	<i>Backward</i>
5	16.55%(0.30%)	17.56%(0.47%)	13.49%(0.24%)	15.49%(0.28%)
10	13.60%(0.31%)	14.92%(0.40%)	12.14%(0.35%)	12.20%(0.33%)
25	13.10%(0.23%)	14.32%(0.48%)	13.11%(0.23%)	11.51%(0.33%)
40	1.88%(0.97%)	4.13%(0.62%)	4.66%(0.53%)	0.06%(0.66%)

Table 2: The error of four methods

N	$K = 100\%$			
	<i>Euler</i>	<i>AES</i>	<i>Truncated</i>	<i>Backward</i>
5	15.79%(0.16%)	18.65%(0.31%)	14.08%(0.24%)	15.97%(0.10%)
10	12.40%(0.20%)	15.94%(0.39%)	12.71%(0.25%)	12.66%(0.20%)
25	11.40%(0.23%)	14.22%(0.30%)	13.07%(0.23%)	11.49%(0.23%)
40	3.61%(1.26%)	3.54%(0.70%)	3.86%(0.74%)	0.46%(0.68%)

the method becomes less sensitive to step-size variations and its advantage diminishes. Nevertheless, it still performs relatively well in terms of computational efficiency. When the number of steps is large, the Backward method outperforms the others in terms of accuracy. However, in terms of runtime, our statistics (for instance, with 40 steps: AES: 0.1114 seconds, Euler: 0.0939 seconds, Truncated: 0.0733 seconds, Backward: 137.9476 seconds) indicate that the backward method is significantly slower, primarily because it relies on the Newton-Raphson method to solve equations. This highlights a potential direction for future improvements, where more efficient numerical schemes or better initial value predictions could accelerate equation solving. In summary, the two new methods we propose both demonstrate clear advantages, and their applicability depends on

Table 3: The error of four methods

N	$K = 150\%$			
	<i>Euler</i>	<i>AES</i>	<i>Truncated</i>	<i>Backward</i>
5	14.72%(0.50%)	17.13%(1.77%)	13.96%(0.85%)	17.32%(1.58%)
10	12.11%(0.34%)	13.69%(0.92%)	13.44%(0.76%)	14.35%(0.61%)
25	11.05%(0.41%)	12.19%(0.48%)	13.48%(0.52%)	13.11%(0.45%)
40	3.85%(1.50%)	2.87%(1.15%)	4.80%(1.35%)	1.44%(1.15%)

the specific context and computational requirements.

We systematically evaluated the numerical performance of the AES method, the Euler method, and the Truncated method proposed in this paper under different values of the volatility parameter \bar{v} . The simulation results reveal a clear and consistent pattern: as \bar{v} increases, the absolute errors (AbsError) of both the AES and Euler methods rise significantly. In contrast, the Truncated method exhibits notable robustness in error control, with its error growth rate remaining lower than that of the conventional AES method and Euler method.

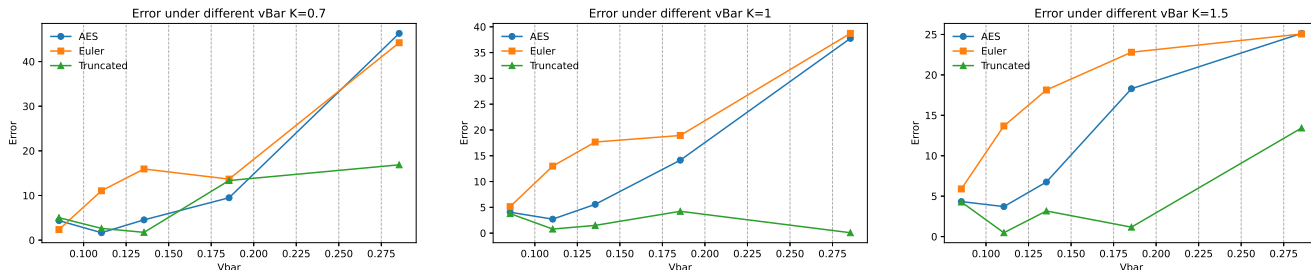


Figure 2: Error under different \bar{v}

An increase in the \bar{v} parameter is financially equivalent to simulating an extreme scenario in which volatility surges sharply and market stress intensifies—similar to the “volatility spikes” observed during financial crises. In such scenarios, the distribution of the underlying asset paths exhibits heavier tails and higher kurtosis, imposing stringent requirements on the numerical accuracy of option-pricing models. As an advanced explicit scheme, the AES method performs highly efficiently under normal market conditions (with moderate \bar{v}). However, its performance is highly sensitive to parameter changes. When \bar{v} increases, the variability of the variance process intensifies, and discretization errors are magnified. The rapid escalation of error indicates that AES is inadequate for stress testing and tail-risk modeling, as it may substantially under- or overestimate option values under extreme market conditions, thereby introducing significant model risk. In contrast, the Truncated (CUT) method exhibits strong numerical stability. Its error increases only marginally with higher \bar{v} , demonstrating reduced sensitivity and greater adaptability to the average magnitude of the volatility process. This robustness arises from its design: by applying appropriate mathematical transformations, the method more effectively captures the complex ge-

ometric characteristics of distribution tails, ensuring that the integral approximation maintains high accuracy even under extreme parameterizations.

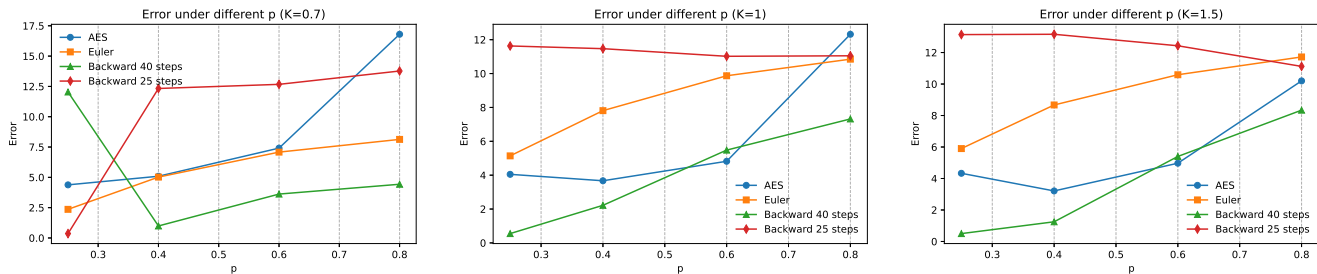


Figure 3: Error under different p

We systematically evaluated the numerical performance of the AES method, the Euler method, and the backward method proposed in this paper under different values of the parameter ppp . The simulation results reveal a clear and consistent pattern: as ppp increases—representing an extreme scenario of model misspecification or a sharp regime shift in market conditions, which is particularly relevant for assessing model performance in out-of-sample settings or stress tests—the calibration errors of all three methods rise to some extent. However, the backward method consistently outperforms the others. Specifically, the implicit (backward) scheme achieves the smallest absolute errors, and its error growth rate remains the flattest, demonstrating strong robustness. Nonetheless, we also observed that the backward method is quite sensitive to the step size. When the number of steps increases from 25 to 40, its calibration accuracy fluctuates significantly. This suggests that careful attention must be paid to step-size selection when employing the backward method. While reducing the step size improves accuracy, it inevitably increases computational time. Therefore, a trade-off must be considered: If computational speed is the priority, the number of steps in the implicit method can be reduced. Within an acceptable error tolerance, this enables fast estimation of risk exposures, allowing practitioners to seize short-lived trading opportunities or implement timely hedging strategies. If accuracy is the priority, particularly in model validation, increasing the number of steps for the same model yields more precise and reliable asset valuation results, which are essential for profit-and-loss analysis.

5 Conclusion

In this work, we explored the numerical challenges associated with simulating the Heston stochastic-local volatility (HSLV) model, with emphasis on the CIR variance process. Traditional methods often face problems with maintaining non-negativity or suffer from weak convergence, limiting their practical use in option pricing applications. By introducing the truncated Euler method and the backward Euler method, we addressed these deficiencies from different perspectives. The truncated Euler method is shown to be strongly convergent and highly stable, particularly when volatility surges and tail risks become more pronounced. Its robustness against parameter changes and moderate computational requirements make it a suitable choice in situations where efficiency and reliability are equally important. On the other hand, the backward Euler method demonstrates

excellent accuracy and the most gentle error growth across different stress scenarios. However, this advantage comes with the trade-off of considerably higher computational cost, as solving implicit equations requires iterative methods such as Newton-Raphson. This observation highlights a crucial practical consideration: the selection of step size. While smaller step sizes improve accuracy, they also increase runtime, making it essential to balance precision against efficiency according to the application context. Overall, our findings suggest that both proposed methods possess distinct advantages. The truncated Euler method offers a pragmatic solution for large-scale simulations and real-time risk management, where computational resources and execution speed are critical. In contrast, the backward Euler method is better suited for stress testing, model validation, and situations where accuracy is paramount, such as profit-and-loss attribution. Together, these approaches enrich the numerical toolkit for HSLV model simulation, offering flexible strategies for practitioners facing different objectives in option pricing and risk management. Future research may focus on accelerating the backward scheme through improved initial value prediction or more efficient iterative solvers, further enhancing its applicability in practice.

6 Appendix: strong convergence of truncated Euler method for CIR model

Proof of Proposition 3.1: For simplicity, we denote $\phi(x) = \frac{\kappa}{2} \left(\frac{\theta}{x} - x \right)$. It is easy to check that

$$|\phi(x) - \phi(y)| \leq \frac{2|\kappa| \vee \kappa\theta}{4} \left(1 + \frac{1}{x^2} + \frac{1}{y^2} \right) |x - y|, \quad (6.1)$$

and

$$(x - y) (\phi(x) - \phi(y)) \leq -\frac{\kappa}{2} |x - y|^2. \quad (6.2)$$

Furthermore,

$$|\phi(\pi_\tau(x)) - \phi(\pi_\tau(y))|^2 \leq C \tau^{-1} |x - y|^2, \quad (6.3)$$

and

$$(x - y) (\phi(\pi_\tau(x)) - \phi(\pi_\tau(y))) \leq -\frac{\kappa}{2} |x - y|^2. \quad (6.4)$$

Next, we continue the proof in two steps.

Step 1: Estimate of $\|L_{t_n}^N - \bar{L}_{t_n}^N\|_{L^2(\Omega; \mathbb{R})}$.

Let $e_n = L_{t_n}^N - \bar{L}_{t_n}^N$, then $e_0 = 0$ and

$$\begin{aligned} e_{n+1} - e_n &= \int_{t_n}^{t_{n+1}} \phi(L_s) ds - \phi(\pi_\tau(\bar{L}_{t_n}^N))\tau \\ &= \int_{t_n}^{t_{n+1}} [\phi(L_s) - \phi(\pi_\tau(L_{t_n}))] ds - \tau \left[\phi(\pi_\tau(L_{t_n})) - \phi(\pi_\tau(\bar{L}_{t_n}^N)) \right]. \end{aligned} \quad (6.5)$$

With the aid of Young's Inequality, (6.3) and (6.4), we get

$$\begin{aligned}
|e_{n+1}|^2 &\leq |e_n|^2 + 2 \left| \int_{t_n}^{t_{n+1}} [\phi(L_s) - \phi(\pi_\tau(L_{t_n}))] ds \right|^2 + 2\tau^2 \left| \phi(\pi_\tau(L_{t_n})) - \phi(\pi_\tau(\bar{L}_{t_n}^N)) \right|^2 \\
&\quad + 2e_n \int_{t_n}^{t_{n+1}} [\phi(L_s) - \phi(\pi_\tau(L_{t_n}))] ds + 2\tau e_n \left[\phi(\pi_\tau(L_{t_n})) - \phi(\pi_\tau(\bar{L}_{t_n}^N)) \right] \\
&\leq (1 + \tau)|e_n|^2 + \left(2 + \frac{1}{\tau} \right) \left| \int_{t_n}^{t_{n+1}} [\phi(L_s) - \phi(\pi_\tau(L_{t_n}))] ds \right|^2 \\
&\quad + 2\tau^2 \left| \phi(\pi_\tau(L_{t_n})) - \phi(\pi_\tau(\bar{L}_{t_n}^N)) \right|^2 + 2\tau e_n \left[\phi(\pi_\tau(L_{t_n})) - \phi(\pi_\tau(\bar{L}_{t_n}^N)) \right] \\
&\leq (1 + C\tau)|e_n|^2 + \left(2 + \frac{1}{\tau} \right) \left| \int_{t_n}^{t_{n+1}} [\phi(L_s) - \phi(\pi_\tau(Y(t_n)))] ds \right|^2.
\end{aligned} \tag{6.6}$$

By iteration, we have

$$|e_{n+1}|^2 \leq C \left(\tau \sum_{i=0}^n |e_i|^2 + \frac{1}{\tau} \sum_{i=0}^n \left| \int_{t_i}^{t_{i+1}} [\phi(L_s) - \phi(\pi_\tau(L_{t_i}))] ds \right|^2 \right). \tag{6.7}$$

Taking expectation on both sides and applying Gronwall's inequality give

$$\mathbb{E} [|e_n|^2] \leq C \frac{1}{\tau} \sum_{i=0}^n \mathbb{E} \left[\left| \int_{t_i}^{t_{i+1}} [\phi(L_s) - \phi(\pi_\tau(L_{t_i}))] ds \right|^2 \right]. \tag{6.8}$$

In the sequence, we bound $\mathbb{E} \left[\left| \int_{t_i}^{t_{i+1}} [\phi(L_s) - \phi(\pi_\tau(L_{t_i}))] ds \right|^2 \right]$. Thanks to the fundamental inequality, we derive

$$\begin{aligned}
&\mathbb{E} \left[\left| \int_{t_i}^{t_{i+1}} [\phi(L_s) - \phi(\pi_\tau(L_{t_i}))] ds \right|^2 \right] \\
&\leq 2\mathbb{E} \left[\left| \int_{t_i}^{t_{i+1}} [\phi(L_s) - \phi(L_{t_i})] ds \right|^2 \right] + 2\tau^2 \mathbb{E} [|\phi(L_{t_i}) - \phi(\pi_\tau(L_{t_i}))|^2].
\end{aligned} \tag{6.9}$$

On one hand, it follows by Itô isometry and moment bounds of $Y(t)$ that

$$\begin{aligned}
&\mathbb{E} \left[\left| \int_{t_i}^{t_{i+1}} [\phi(L_s) - \phi(L_{t_i})] ds \right|^2 \right] = \mathbb{E} \left[\left| \int_{t_i}^{t_{i+1}} \int_{t_i}^s d\phi(L_r) ds \right|^2 \right] \\
&= \mathbb{E} \left[\left| \int_{t_i}^{t_{i+1}} (t_{i+1} - r) \phi'(L_r) \phi(L_r) dr + \int_{t_i}^{t_{i+1}} \frac{\sigma}{2} (t_{i+1} - r) \phi'(L_r) dW_r \right|^2 \right] \\
&\leq C \left(\mathbb{E} \left[\left| \int_{t_i}^{t_{i+1}} (t_{i+1} - r) \phi'(L_r) \phi(L_r) dr \right|^2 \right] + \mathbb{E} \int_{t_i}^{t_{i+1}} |(t_{i+1} - r) \phi'(L_r)|^2 dr \right) \\
&\leq C \tau^4 + C \tau^3.
\end{aligned} \tag{6.10}$$

On the other hand, note that

$$\begin{aligned}
|\phi(L_{t_i}) - \phi(\pi_\tau(L_{t_i}))|^2 &\leq C \left(1 + \frac{1}{|L_{t_i}|^4} + \frac{1}{|\pi_\tau(L_{t_i})|^4} \right) |L_{t_i} - \pi_\tau(L_{t_i})|^2 \\
&\leq C \left(1 + \frac{1}{|L_{t_i}|^4} \right) |L_{t_i} - b\tau^{\frac{1}{4}}|^2 \chi_{\{L_{t_i} < b\tau^{\frac{1}{4}}\}} \\
&\leq C\tau^{\frac{1}{2}} (1 + |L_{t_i}|^{-4}) \chi_{\{L_{t_i} < b\tau^{\frac{1}{4}}\}}.
\end{aligned} \tag{6.11}$$

Using Hölder's inequality and Chebyshev's inequality leads to

$$\begin{aligned}
2\tau^2 \mathbb{E} [|\phi(L_{t_i}) - \phi(\pi_\tau(L_{t_i}))|^2] &\leq C\tau^{\frac{5}{2}} \left(\mathbb{P}\{L_{t_i} < b\tau^{\frac{1}{4}}\} + \mathbb{E} \left[|L_{t_i}|^{-4} \chi_{\{L_{t_i} < b\tau^{\frac{1}{4}}\}} \right] \right) \\
&\leq C\tau^{\frac{5}{2}} \left(\mathbb{P} \left\{ L_{t_i}^{-1} > (b\tau^{\frac{1}{4}})^{-1} \right\} + \mathbb{E} [|L_{t_i}|^{-6}]^{\frac{2}{3}} \left[\mathbb{P} \left\{ L_{t_i}^{-1} > (b\tau^{\frac{1}{4}})^{-1} \right\} \right]^{\frac{1}{3}} \right) \\
&\leq C\tau^3.
\end{aligned} \tag{6.12}$$

Hence,

$$\mathbb{E} [|e_n|^2] \leq C \frac{1}{\tau} \sum_{i=0}^n \tau^3 \leq C\tau. \tag{6.13}$$

Step 2: Estimate of $\|L_{t_n} - \bar{L}_{t_n}^N\|_{L^2(\Omega; \mathbb{R})}$.

Introduce an auxiliary process $\bar{L}_{t_n} = \pi_\tau(Y_{t_n})$, then

$$\mathbb{E} \left[\left| \bar{L}_{t_n}^N - L_{t_n} \right|^2 \right] \leq 2\mathbb{E} \left[\left| \bar{L}_{t_n}^N - \bar{L}_{t_n} \right|^2 \right] + 2\mathbb{E} \left[\left| \bar{L}_{t_n} - L_{t_n} \right|^2 \right]. \tag{6.14}$$

On one hand, by the property of π_τ , we have

$$\mathbb{E} \left[\left| \bar{L}_{t_n}^N - \bar{L}_{t_n} \right|^2 \right] \leq \mathbb{E} \left[\left| L_{t_n}^N - L_{t_n} \right|^2 \right] \leq C\tau. \tag{6.15}$$

On the other hand, following the similar manner of the treatment of (6.11) and (6.12), and using Chebyshev's inequality arrives at

$$\mathbb{E} \left[\left| \bar{L}_{t_n} - L_{t_n} \right|^2 \right] \leq C\tau^2. \tag{6.16}$$

Therefore, we finish the proof. \square

References

- [1] L. B. G. Andersen and V. V. Piterbarg. Moment explosions in stochastic volatility models. *Finance and Stochastics*, 11:29–50, 2007.
- [2] J. Andreasen and B. Høge. Volatility interpolation. *Risk Magazine*, 3:86–89, 2011.

- [3] M. Broadie and O. Kaya. Exact simulation of stochastic volatility and other affine jump diffusion processes. *Operations Research*, 54(2):217–231, 2006.
- [4] J. Cox, J. Ingersoll, and S. Ross. A theory of the term structure of interest rates. *Econometrica*, 53(2):385–407, 1985.
- [5] A. Cozma, M. Mariapragassam, and C. Reisinger. Convergence of an Euler scheme for a hybrid stochastic-local volatility model with stochastic rates in foreign exchange markets. *SIAM Journal on Financial Mathematics*, 9(1):127–170, 2018.
- [6] A. Cozma and C. Reisinger. Strong order 1/2 convergence of full truncation Euler approximations to the Cox-Ingersoll-Ross process. *IMA Journal of Numerical Analysis*, 2018.
- [7] S. Dereich, A. Neuenkirch, and L. Szpruch. An Euler-type method for the strong approximation of the Cox-Ingersoll-Ross process. *Proceedings of the Royal Society A: Mathematical, Physical and Engineering Sciences*, 468(2140):1105–1115, 2012.
- [8] E. Derman and I. Kani. Stochastic implied trees: Arbitrage pricing with stochastic term and strike structure of volatility. *International Journal of Theoretical and Applied Finance*, 1(1):61–110, 1998.
- [9] B. Dupire. Pricing with a smile. *Risk Magazine*, 7(1):18–20, 1994.
- [10] X. Gao, J. Wang, Y. Wang and H. Yang. The truncated Euler-Maruyama method for CIR model driven by fractional Brownian motion. *Statistics & Probability Letters*, 189:109573, 2022.
- [11] B. Engelmann, F. Koster and D. Oeltz. Calibration of the Heston stochastic local volatility model: A finite volume scheme, *SSRN Electronic Journal*, 2011.
- [12] J. Guyon and P. Henry-Labordère. The smile calibration problem solved. *SSRN.1885032*, 2011.
- [13] S. L. Heston. A closed-form solution for options with stochastic volatility with applications to bond and currency options. *The Review of Financial Studies*, 6:327–343, 1993.
- [14] W. Hu and J. Zhou. Backward simulation methods for pricing American options under the CIR process. *Quantitative Finance*, 17(11):1683–1695, 2017.
- [15] M. Jex, R. Henderson, and D. Wang. Pricing exotics under the smile. *Risk*, 12:72–75, 1999.
- [16] A. Lipton. The vol smile problem. *Risk*, 15:61–65, 2002.
- [17] R. Rebonato. Volatility and Correlation: In the Pricing of Equity, FX, and Interest-rate Options. New York: John Wiley & Sons, Ltd. 1999.
- [18] Y. Ren, D. Madan, and M. Qian Qian. Calibrating and pricing with embedded local volatility models. *Risk*, 20:138–143, 2007.

- [19] M. J. Ruijter and C. W. Oosterlee. Two-dimensional Fourier Cosine series expansion method for pricing financial options. *SIAM Journal on Scientific Computing*, 34(5):B642–B671, 2012.
- [20] R. Schöbel and J. Zhu. Stochastic volatility with an Ornstein–Uhlenbeck process: An extension. *European Finance Review*, 3:23–46, 1999.
- [21] Y. Tian, Z. Zhu, G. Lee, F. Klebaner, and K. Hamza. Calibrating and pricing with a stochastic–local volatility model. *Journal of Derivatives*, 22:21–39, 2015.
- [22] A. W. Van Der Stoep, L. A. Grzelak and C. W. Oosterlee. The Heston stochastic-local volatility model: efficient Monte Carlo simulation. *International Journal of Theoretical and Applied Finance*, 17(7):1450045, 2014.